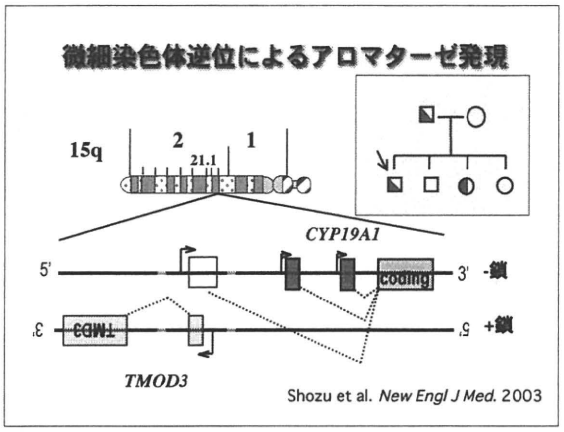

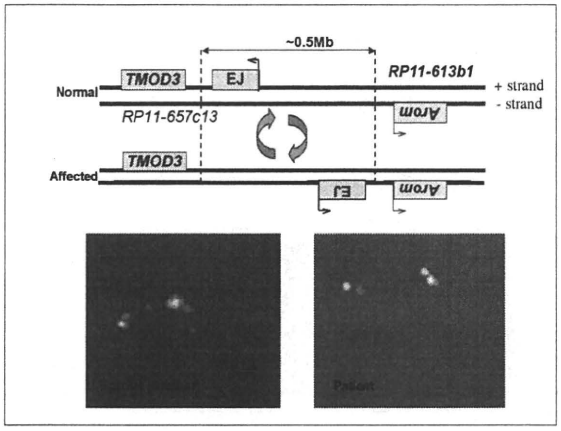

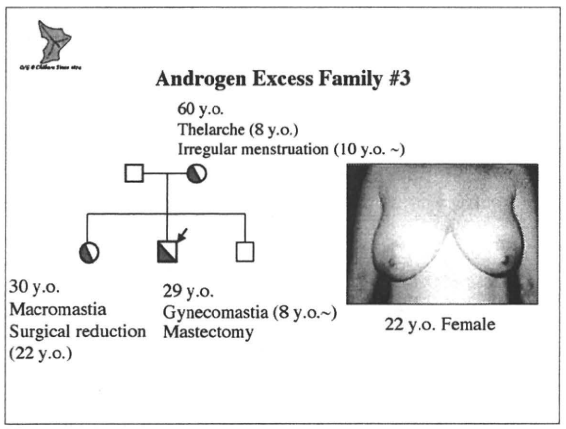

アロマターゼ過剰症の遺伝子異常

	患者	表現型	遺伝子異常
#1	1 男	女性化乳房・思春期早発・低身長	Inversion of **TMOD3** promoter
#2	2 男	女性化乳房・思春期早発・低身長	Inversion of **CGNL1** promoter
#3	1 男	女性化乳房 低身長	Inversion of **MAPK6** promoter
	2 女	巨大乳房・早期の乳房発育・不規則月経、不正出血 低慎重	
#4	1 男	女性化乳房 正常身長	Inversion of **TLN2** promoter

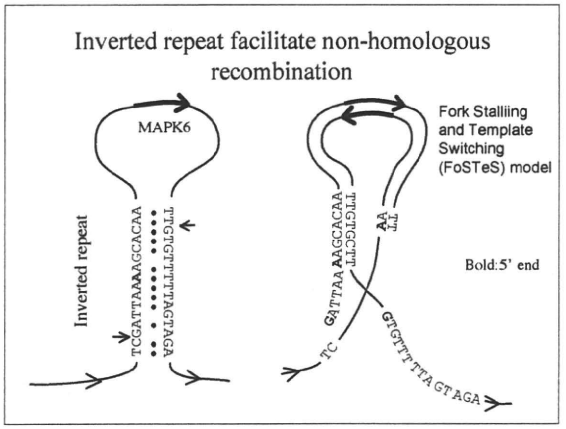

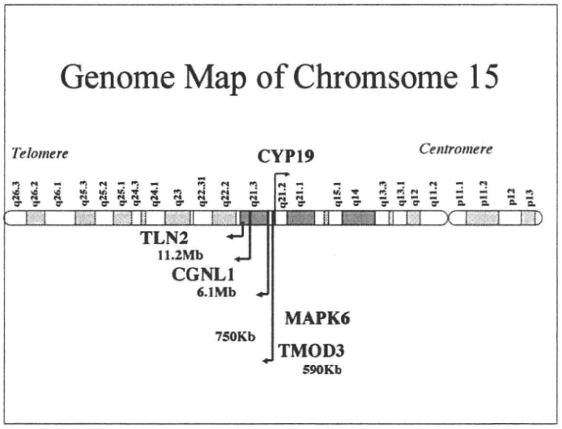

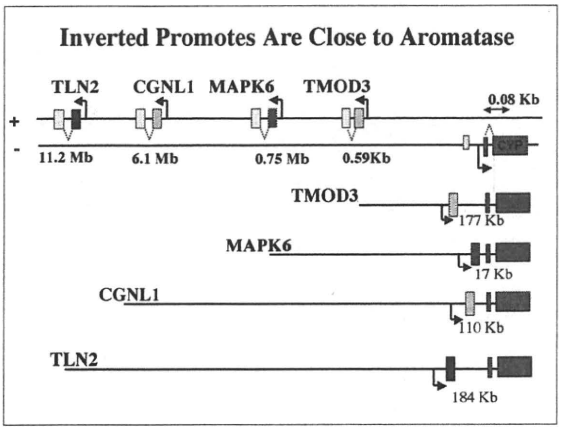
Inverted Promotes Are Close to Aromatase
TLN2
CGNL1
MAPK6
TMOD3
0.08 Kb
+
-
11.2 Mb
6.1 Mb
0.75 Mb
0.59Kb
TMOD3
177 Kb
MAPK6
17 Kb
CGNL1
110 Kb
TLN2
184 Kb

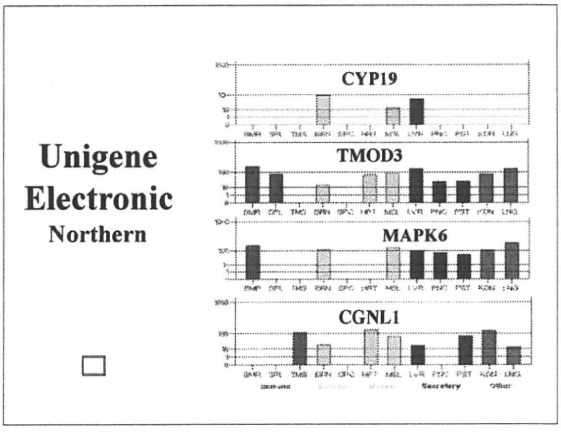
Unigene
Electronic
Northern
CYP19
TMOD3
MAPK6
CGNL1

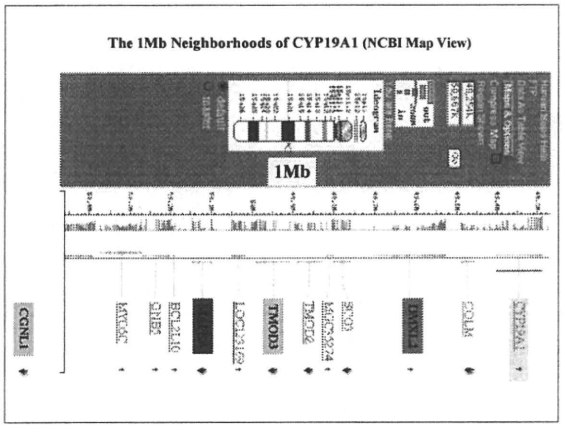
The 1Mb Neighborhoods of CYP19A1 (NCBI Map View)
1Mb
CGNL1
TMOD3
CYP19A1

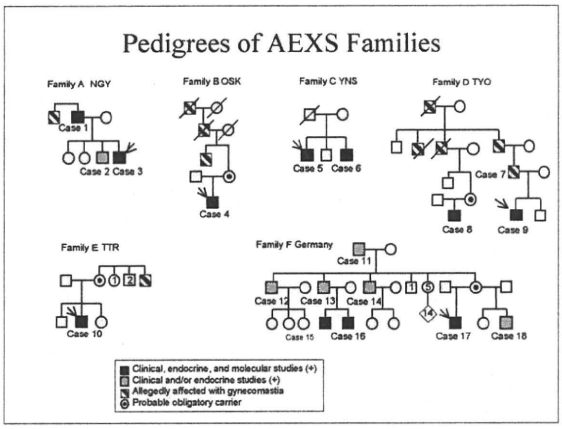
Pedigrees of AEXS Families
Family A NGY
Family B OSK
Family C YNS
Family D TYO
Family E TTR
Family F Germany
Clinical, endocrine, and molecular studies (+)
Clinical and/or endocrine studies (+)
Allegedly affected with gynecomastia
Probable obligatory carrier

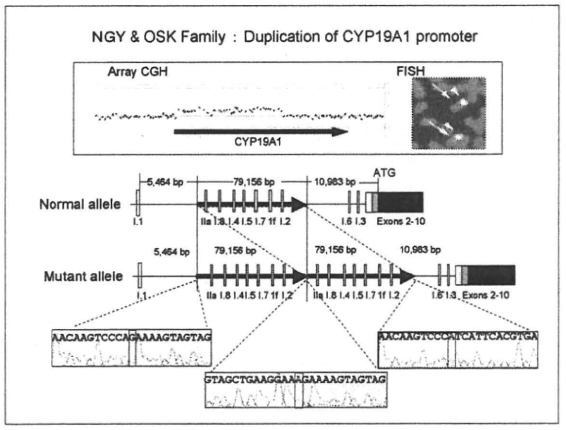
NGY & OSK Family : Duplication of CYP19A1 promoter
Array CGH
FISH
CYP19A1
Normal allele
Mutant allele
5,464 bp
79,156 bp
10,983 bp
ATG
Exons 2-10

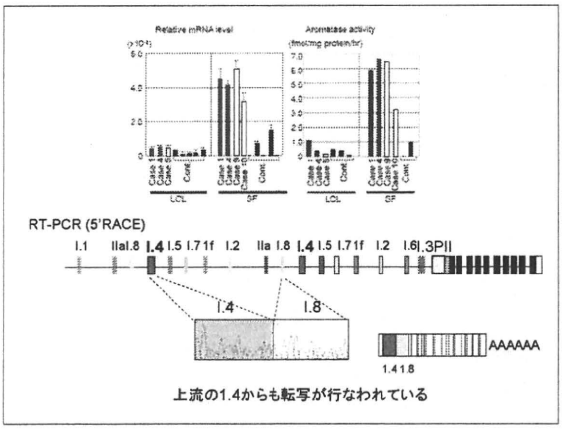
RT-PCR (5'RACE)
AAAAAA
上流の1.4からも転写が行なわれている

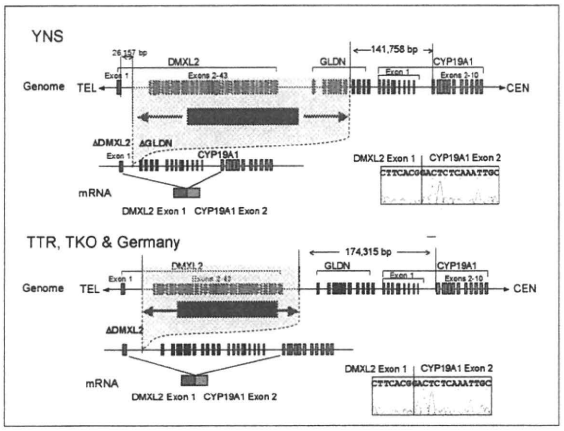
YNS
Genome
TEL
CEN
DMXL2
GLDN
CYP19A1
Exons 2-43
Exons 2-10
141,758 bp
ΔDMXL2
ΔGLDN
mRNA
DMXL2 Exon 1 CYP19A1 Exon 2
TTR, TKO & Germany
174,315 bp

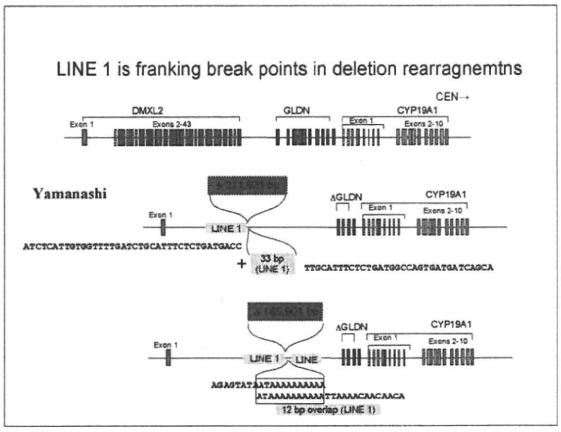
LINE 1 is franking break points in deletion rearragnemtns
CEN→
DMXL2
GLDN
CYP19A1
Yamanashi
LINE 1
33 bp (LINE 1)
12 bp overlap (LINE 1)

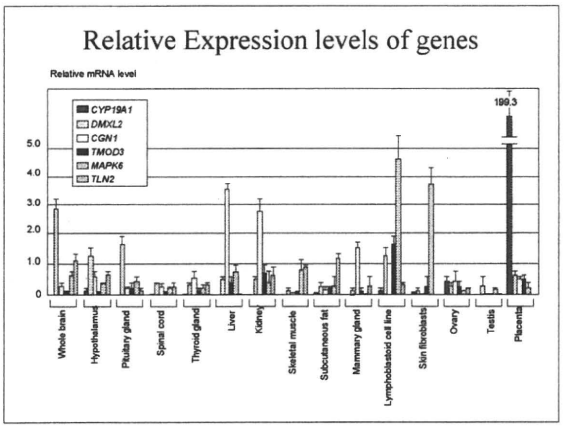
Relative Expression levels of genes
Relative mRNA level
CYP19A1
DMXL2
CGN1
TMOD3
MAPK6
TLN2
199.3
Whole brain
Hypothalamus
Pituitary gland
Spinal cord
Thyroid gland
Liver
Kidney
Skeletal muscle
Subcutaneous fat
Mammary gland
Lymphoblastoid cell line
Skin fibroblasts
Ovary
Testis
Placenta

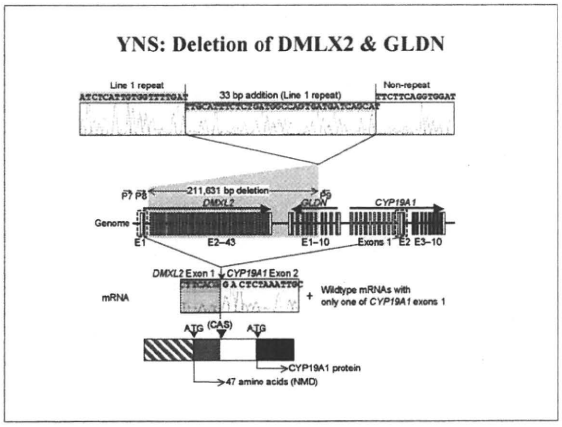
YNS: Deletion of DMLX2 & GLDN
Line 1 repeat
33 bp addition (Line 1 repeat)
Non-repeat
211,631 bp deletion
Genome
DMXL2
GLDN
CYP19A1
E1
E2–43
E1–10
Exons 1 E2 E3–10
mRNA
Wildtype mRNAs with only one of CYP19A1 exons 1
ATG (CAS)
ATG
CYP19A1 protein
47 amino acids (NMD)

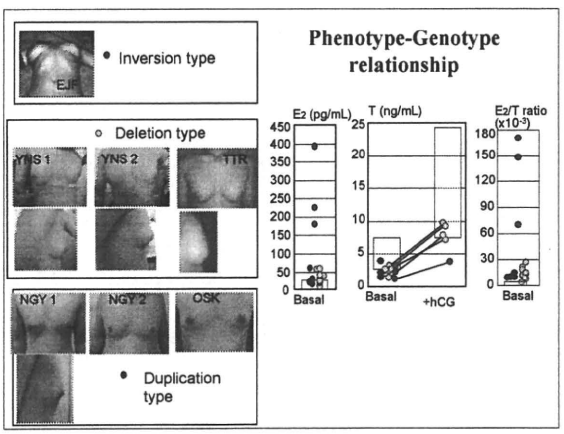
Inversion type
Deletion type
YNS 1
YNS 2
TTR
NGY 1
NGY 2
OSK
Duplication type
Phenotype-Genotype relationship
E2 (pg/mL)
T (ng/mL)
E2/T ratio (x10-3)
Basal
+hCG

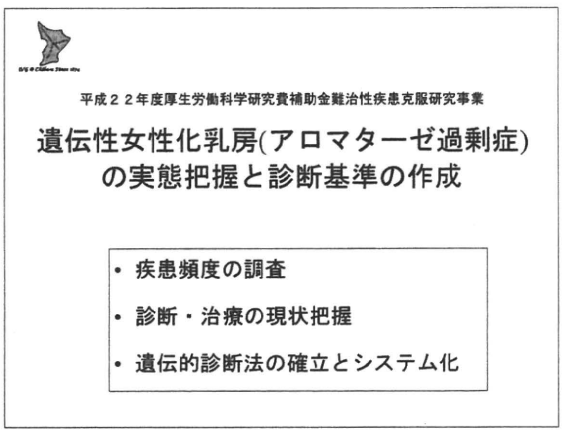
平成２２年度厚生労働科学研究費補助金難治性疾患克服研究事業
遺伝性女性化乳房(アロマターゼ過剰症)の実態把握と診断基準の作成
• 疾患頻度の調査
• 診断・治療の現状把握
• 遺伝的診断法の確立とシステム化

医学中央雑誌 “女性化乳房”

1983-2010
(女性化乳房/TH or 女性化乳房/AL)
575件

2010.5.1

女性化乳房なし
症例報告でない
重複報告
275件

300件

国内文献の分類

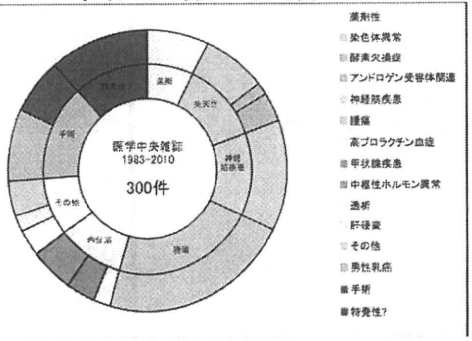

診療科

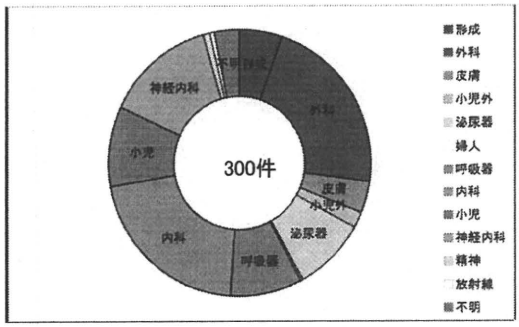

年齢別

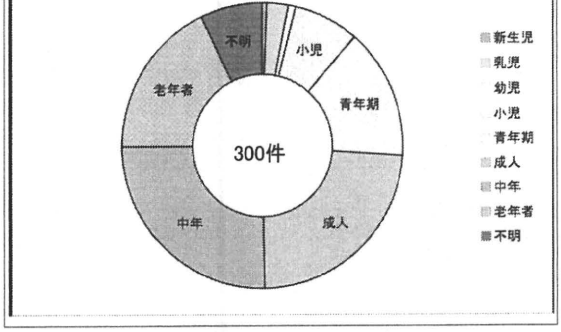

特発性疑い例_診療科

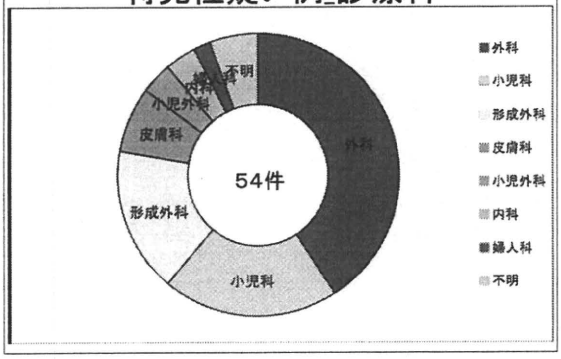

特発性疑い例_年齢別

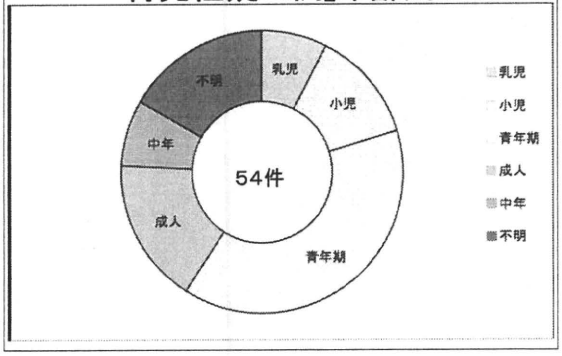

報告例のまとめ

- 国内文献では、特発性症例が54例報告されていた。
- 国外文献を含めて、1977年以降に15家系20症例が報告されている。
- 女性化乳房症は、25歳までに発症し、ほとんどの症例で家系歴が認められた。

国外文献

- 1980-2000年の20年間に単一地域医療センターで経験したGynecomastiaは581例あり、そのうち29例が思春期症例であった。
- 29症例中、2例にのみ家族歴があり、エストロゲン高値が認められた。身長加速の促進と骨年令の促進も見られた。乳房発育は、テストステロン投与が開始されるまで継続して認められた。
- このほかの27例には、いずれの症状も認められなかった。乳房の大きさや発症時期、乳腺の形態から、AEXSとの区別はできなかった。肥満が1/3に認められた。血中エストロゲン値は、年齢相当であった。27例では原因が不明で、特発性とされた。
- 以上より、思春期の女性化乳房症は、ほとんどが特発性（原因不明）で、５%に家族歴・エストロゲン高値がみられるAEXSが認められる。このＡＥＸＳには、エストロゲン高値によるものと推察される発育および骨年令の促進が観察される。

Prepubertal gynaecomastia: aetiology, course and outcome.
Einav-Bachar R, et al. Clin Endocrinol (Oxf). 2004 Jul;61(1):55-60.

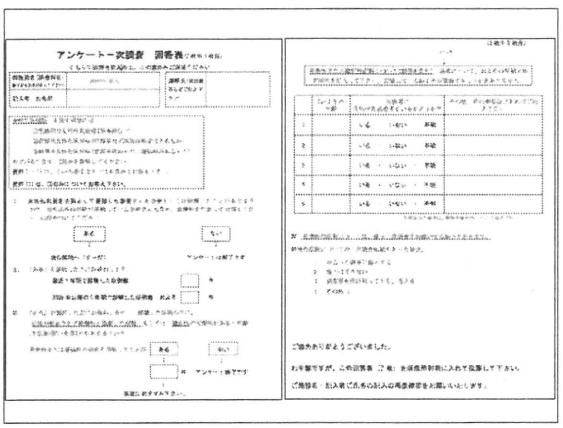

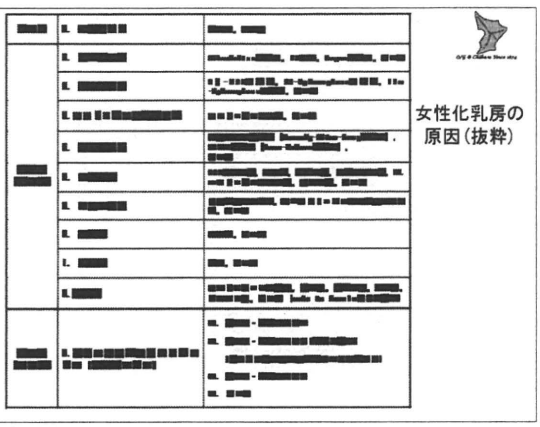
女性化乳房の原因（抜粋）

アンケートの返信内訳

- 発送数:2817通
- 返信数:977通
- 有りとの返信:186例
- 有りとの延べ症例数:304例
- 明らかな2次性巨大乳房症:9例

- 検討症例:295例

一次調査結果

カテゴリー	家族歴	発症年齢	遺伝性女性化乳房症の可能性	患者数
1a	あり	<25歳	高い	23
1b	不明 or なし	<25歳	ある（否定できない）	146
2-X	その他	その他	低い or ない	135
			合計	304

発症年齢別患者数（一次調査）

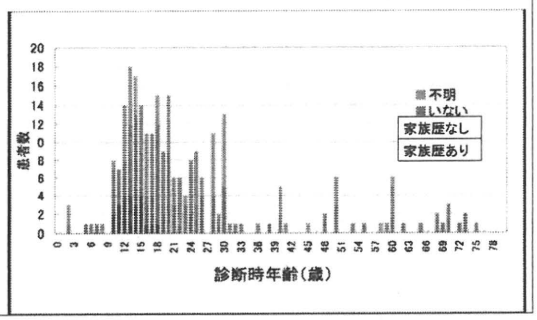

遺伝性女性化乳房症

- CYP19A1近傍の遺伝子組み換えにより、近傍遺伝子プロモーターがCYP19A1にリクルートされたことにより発現亢進をきたしたもの。
- 常染色体優性で、男性では思春期より女性化乳房症を発症する。
- 遺伝子型と表現型には関連がある。

Summary of CYP19A1 Mutations

Genotype	Heredity	Symptome	Detection	No. of subtypes	Activity/ whole body	Proposed Mechanism
Normal		-		-	1	
Point mutation	AR	Deficiency	Sequencing	~20	0~0.2	Replication error
Inversion	AD	Excess	5'-RACE	4	10~50	NAHR (FoSTeS)
Deletion	AD	Excess	CGH array	2	5~10	NAHR (LINE 1)
Duplication	AD	Excess	CGH array	1	1.5	NAHR

Collaborators

National Research Institute for Child health and Development, Tokyo
Maki Fukami, Tsutomu Ogata, Reiko Horikawa

Chiba University Hirokazu Usui
Nothwestern University Serdar E. Bulun
Siby Sebastian
Tohoku University Kazuto Takayama
Kanazawa University Masashi Demura
Fujita Heath University Nobuhiro Harada
Osaka University Shinzaburo Noguchi
Josai University Chizuko Yokota
Tottori University Keiichi Hanaki

Nagoya Daini Red Cross Hospital Takagi H
Osaka Police Hospital Nishigaki T
University-Childrens' Hospital Binder G
University of Yamanashi Ohyama K

遺伝性女性化乳房症
Aromatase Excess Syndrome
診断基準の策定（暫定）

- 明らかな2次性女性化乳房を除く、思春期発症の女性化乳房症
- 遺伝性がある
- E1　>30pg/mlのことが多い
- Tは正常下限か低値
- E2/TもしくはE1/T　> 10(5)

Ⅳ. 研究成果の刊行物・別刷

J Clin Endocrin Metab. First published ahead of print April 6, 2011 as doi:10.1210/jc.2011-0145

Aromatase Excess Syndrome: Identification of Cryptic Duplications and Deletions Leading to Gain of Function of *CYP19A1* and Assessment of Phenotypic Determinants

Maki Fukami, Makio Shozu, Shun Soneda, Fumiko Kato, Akemi Inagaki, Hiroshi Takagi, Keiichi Hanaki, Susumu Kanzaki, Kenji Ohyama, Tomoaki Sano, Toshinori Nishigaki, Susumu Yokoya, Gerhard Binder, Reiko Horikawa, and Tsutomu Ogata

Department of Molecular Endocrinology (M.F., S.S., F.K., T.O.), National Research Institute for Child Health and Development, Tokyo 157-8535, Japan; Department of Reproductive Medicine (M.S.), Graduate School of Medicine, Chiba University, Chiba 206-8670, Japan; Department of Diabetes and Endocrinology (A.I., H.T.), Nagoya Second Red Cross Hospital Nagoya 466-8650, Japan; Department of Women's and Children's Family Nursing (K.H.) and Division of Pediatrics and Perinatology (S.K.), Tottori University, Yonago 683-8503, Japan; Department of Pediatrics (K.O., T.S.), Interdisciplinary Graduate School of Medicine and Engineering, University of Yamanashi, Chuo 408-3898, Japan; Department of Pediatrics (T.N.), Osaka Police Hospital, Osaka 543-0035, Japan; Department of Medical Subspecialties (S.Y., R.H.), National Medical Center for Children and Mothers, Tokyo 157-8535, Japan; and Pediatric Endocrinology Section (G.B.), University Children's Hospital, Tuebingen 72076, Germany

Context: Aromatase excess syndrome (AEXS) is a rare autosomal dominant disorder characterized by gynecomastia. Although cryptic inversions leading to abnormal fusions between *CYP19A1* encoding aromatase and its neighboring genes have been identified in a few patients, the molecular basis remains largely unknown.

Objective: The objective of the study was to examine the genetic causes and phenotypic determinants in AEXS.

Patients: Eighteen affected males from six families participated in the study.

Results: We identified three types of heterozygous genomic rearrangements, *i.e.* a 79,156-bp tandem duplication involving seven of 11 noncoding *CYP19A1* exons 1, a 211,631-bp deletion involving exons 2–43 of *DMXL2* and exons 5–10 of *GLDN*, and a 165,901-bp deletion involving exons 2–43 of *DMXL2*. The duplicated exon 1 functioned as transcription start sites, and the two types of deletions produced the same chimeric mRNA consisting of *DMXL2* exon 1 and *CYP19A1* coding exons. The *DMXL2* exon 1 harbored a translation start codon, and the *DMXL2/CYP19A1* chimeric mRNA was identified in only 2–5% of *CYP19A1*-positive transcripts. This was in contrast to the inversion-mediated chimeric mRNA that had no coding sequence on the fused exon 1 and accounted for greater than 80% of *CYP19A1*-positive transcripts. *CYP19A1* was expressed in a limited number of tissues, whereas its neighboring genes involved in the chimeric mRNA formation were expressed widely.

Conclusions: This study provides novel mechanisms leading to gain of function of *CYP19A1*. Furthermore, it appears that clinical severity of AEXS is primarily determined by the tissue expression pattern of relevant genes and by the structural property of promoter-associated exons of chimeric mRNA. (***J Clin Endocrinol Metab* 96: 0000–0000, 2011**)

ISSN Print 0021-972X ISSN Online 1945-7197
Printed in U.S.A.

doi: 10.1210/jc.2011-0145 Received January 18, 2011. Accepted March 22, 2011.

Abbreviations: AEXS, Aromatase excess syndrome; CGH, comparative genomic hybridization; E_2, estradiol; FISH, fluorescence *in situ* hybridization; hCG, human chorionic gonadotropin; LCL, lymphoblastoid cell line; NMD, nonsense-mediated mRNA decay; RACE, rapid amplification of cDNA ends; SF, skin fibroblast; T, testosterone.

Aromatase is a cytochrome P450 enzyme that plays a crucial role in the estrogen biosynthesis (1). It catalyzes the conversion of Δ4-androstendione into estrone and that of testosterone (T) into estradiol (E_2) in the placenta and ovary as well as in other tissues such as the fat, skin, bone, and brain (1). It is encoded by *CYP19A1* consisting of at least 11 noncoding exons 1 and nine coding exons 2–10 (Supplemental Fig. 1, published on The Endocrine Society's Journals Online web site at http://jcem.endojournals.org) (2, 3). Each exon 1 is accompanied by a tissue-specific promoter and is spliced alternatively onto a common splice acceptor site at exon 2, although some transcripts are known to contain two of the exons 1, probably due to a splice error (2, 4). Of the 11 exons 1, exon I.4 appears to play a critical role in the regulation of estrogen biosynthesis in males because this exon contains a major promoter for extragonadal tissues including the skin and fat (2).

Excessive *CYP19A1* expression causes a rare autosomal dominant disorder known as aromatase excess syndrome (AEXS) (5–8). AEXS is characterized by pre- or peripubertal onset gynecomastia, advanced bone age from childhood to the pubertal period, and short adult height in affected males (5–8). Affected females may show several clinical features such as macromastia, precocious puberty, irregular menses, and short adult height (6–8). In this regard, previous studies have identified four heterozygous cryptic inversions around *CYP19A1* in patients with AEXS (5, 8). Each inversion results in the formation of a chimeric gene consisting of a noncoding exon(s) of a neighboring gene (*CGNL1*, *MAPK6*, *TMOD3*, or *TLN2*) and coding exons of *CYP19A1*. Because this condition is predicted to cause aberrant *CYP19A1* expression in tissues in which each neighboring gene is expressed, such inversions have been regarded to be responsible for AEXS (5, 8).

However, such inversions have been revealed only in a few patients with AEXS, and, despite extensive studies, no other underlying genetic mechanisms have been identified to date (6, 8–10). Here we report novel genomic rearrangements in AEXS and discuss primary phenotypic determining factors in AEXS.

Patients and Methods

Patients

This study was approved by the Institutional Review Board Committee at the National Center for Child Health and Development and was performed after obtaining informed consent. We examined 18 male patients aged 8–69 yr (cases 1–18) from six unrelated families A-F (Fig. 1A). The probands were ascertained by bilateral gynecomastia (Fig. 1B) and the remaining 12 males by familial studies. Ten other males allegedly had gynecomastia. There were four obligatory carrier females.

Phenotypic assessment showed pre- or peripubertal onset gynecomastia in all cases, small testes and fairly preserved masculinization in most cases, obvious or relative tall stature in childhood and grossly normal or relative short stature in adulthood, and age-appropriate or mildly advanced bone ages (Table 1) (for detailed actual data, see Supplemental Table 1). Such clinical features, especially gynecomastia, tended to be milder in cases 1–4 from families A and B than in the remaining cases from families C-F. Fertility or spermatogenesis was preserved in all adult cases (≥20 yr). In addition, the obligatory carrier females from families B and D had apparently normal phenotype, and such females from families E and F exhibited early menarche (9.0 yr) and short adult stature (−2.8 SD), respectively.

Blood endocrine studies revealed that LH values were grossly normal at the baseline and variably responded to GnRH stimulation, whereas FSH values were low at the baseline and responded poorly to GnRH stimulation, even after preceding GnRH priming (Table 1) (for detailed actual data, see Supplemental Table 1) (see also Fig. 1C for the cases aged ≥15 yr). Δ^4-Androstendione, T, and dihydrotestosterone values were low or normal. A human chorionic gonadotropin (hCG) test indicated relatively low but normal T responses in five young cases. In most cases, estrone values were elevated, E_2 values were normal or elevated, and E_2/T ratios were elevated. These endocrine data were grossly similar among cases 1–18.

Aromatase inhibitor (anastrozole, 1 mg/d) was effective in all the four cases treated (Supplemental Table 1) (see also Fig. 1C for cases aged ≥15 yr). Gynecomastia was mitigated within 6 months of treatment, and endocrine data were ameliorated within 1 month of treatment.

Primers

Primers used in this study are shown in Supplemental Table 2.

CYP19A1 mRNA levels and aromatase activities

We analyzed relative mRNA levels of *CYP19A1* and catalytic activities of aromatase in skin fibroblasts (SF) and lymphoblastoid cell lines (LCL). mRNA were extracted by a standard method and were subjected to RT-PCR using a high capacity RNA-to-cDNA kit (Life Technologies, Carlsbad, CA). A relative amount of *CYP19A1* mRNA against *B2M* was determined by the real-time PCR method using the Taqman gene expression assay on ABI PRISM 7500fast (Life Technologies) (assay no. Hs00903411_m1 for *CYP19A1* and Hs99999907_m1 for *B2M*). PCR was performed in triplicate. Aromatase activity was determined by a tritium incorporation assay (11). In brief, the samples were incubated with androstenedione-2-^{3}H for 2 h, and ^3H_2O in the supernatant of the culture media was measured with a scintillation counter LSC-5100 (Aloka, Tokyo, Japan).

Sequence analysis of *CYP19A1*

Leukocyte or SF genomic DNA samples from the six probands and additional four male patients (Fig. 1A) were PCR amplified for the coding exons 2–10 and their flanking splice sites of *CYP19A1*. Subsequently the PCR products were subjected to direct sequencing from both directions on CEQ 8000 autosequencer (Beckman Coulter, Fullerton, CA).

Genome structure analysis

Oligonucleotide array-based comparative genomic hybridization (CGH) analyses were carried out using a custom-built

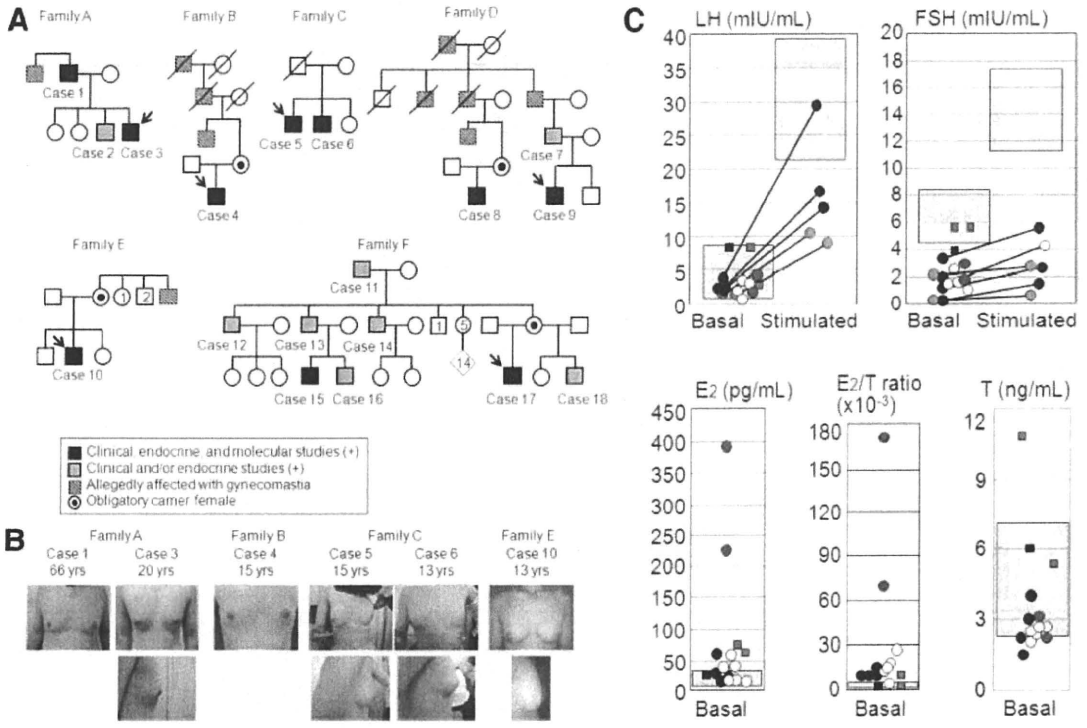

FIG. 1. Summary of clinical data. A, Pedigrees of six families with patients exhibiting AEXS-compatible phenotype. Families A–E are of Japanese origin, and family F is of German origin. Cases from families A–D were hitherto unreported, whereas those from families E and F have previously been described as having AEXS phenotypes (6, 8). B, Gynecomastia of six cases. C, Endocrine data in cases 15 yr of age or older. The *black*, *white*, and *red colors* represent the data in cases of the duplication, the deletion, and the inversion types, respectively; the *blue color* indicates the data of GnRH test after GnRH priming in two cases of the duplication type. The data at the time of diagnosis are denoted by *circles*, and those on aromatase inhibitor (anastrozole) treatment (1 mg/d in the duplication and the deletion types and 2–4 mg/d in the inversion types) are depicted by *squares*. The *light purple areas* represent the normal reference ranges.

oligo-microarray containing 90,000 probes for the 15q11.2-q26.3 region and approximately 10,000 reference probes for other chromosomal region (2 × 105K format, design identification 026533) (Agilent Technologies, Palo Alto, CA). The procedure was as described in the manufacturer's instructions. Fluorescence *in situ* hybridization (FISH) analysis was performed for lymphocyte or SF metaphase spreads, using long PCR products (FISH probes 1 and 2) for rearranged regions and CEP 15 probe for *D15Z4* used as an internal control (Abbott, Abbott Park, IL). The FISH probes 1 and 2 were labeled with digoxigenin and detected by rhodamine antidigoxigenin, and the CEP 15 probe was detected according to the manufacturer's protocol.

Characterization of the duplications and deletions

The duplication junctions were determined by direct sequencing for standard PCR products obtained with a variety of combinations of primers hybridizing to different positions within the *CYP19A1* exons 1 region. The deletion junctions were identified by direct sequencing of the long PCR products obtained with primer pairs flanking the deletions. The sizes of duplications and the deletions were determined by comparing obtained sequences with NT_010194 sequences at the National Center for Biotechnology Information Database (http://www.ncbi.nlm.nih.gov/; Bethesda, MD). The presence or absence of repeat sequences around the breakpoints was examined with Repeatmasker (http://www.repeatmasker.org).

For mRNA analysis, we preformed 5′-rapid amplification of cDNA ends (RACE) using a SMARTER RACE cDNA amplification kit (Takara Bio, Ohtsu, Japan). For both duplications and deletions, first PCR was carried out using the forward primer mix provided in the kit (Universal primer A mix) and an antisense reverse primer specific to *CYP19A1* exon 3 (RACE Rev). Second PCR was carried out for diluted products of the first PCR, using the nested forward primer of the kit (Nested universal primer A) and a reverse primer for *CYP19A1* exon 2 (Nested Rev). For duplications, furthermore, second PCR was also performed using various combinations of primers hybridizing to each *CYP19A1* exon 1. Subsequently PCR products were subcloned into TOPO cloning vector (Life Technologies) and subjected to direct sequencing. Then, the obtained sequences were examined with BLAST Search (National Center for Biotechnology Information). The presence or absence of promoter-compatible sequences was analyzed with the University of California, Santa Cruz, genome browser (http://genome.ucsc.edu/).

Relative mRNA levels of *CYP19A1* and its neighboring genes

We investigated relative mRNA levels of *CYP19A1* and *DMXL2* as well as those of *CGNL1*, *MAPK6*, *TMOD3*, and *TLN2* involved in the previously reported cryptic inversions (5, 8) in various human tissues. In this experiment, cDNA of SF and LCL were obtained from control males, and the remaining human cDNA samples were purchased from Life Technologies or Takara Bio. Relative quantification of mRNA against *TBP* was carried out using Taqman gene expression assay kit

TABLE 1. Summary of clinical studies in male patients with aromatase excess syndrome[a]

	Present study						Previous studies			
	Family A	Family B	Family C	Family D	Family E	Family F	Family 1	Family 2	Sporadic	
Cases	Cases 1–3	Case 4	Cases 5–6	Cases 7–9	Case 10	Cases 11–18	Two cases[b]	Proband[c]	Patient 1	Patient 2
Mutation type	Duplication	Duplication	Deletion	Deletion	Deletion	Deletion	Inversion	Inversion	Inversion	Inversion
Phenotypic findings										
Gynecomastia	Yes (mild)	Yes (mild)	Yes (moderate)	Yes (moderate)	Yes (moderate)	Yes (moderate)	Yes (severe)	Yes (severe)	Yes (severe)	Yes (severe)
Pubertal defect	Yes (mild)	Yes (mild)	Yes (mild)	No	No	Yes (mild)	N.D.	Yes (mild)	No	N.D.
Short adult height	No	No	N.D.	No	N.D.	No	Yes	N.D.	Yes	N.D.
Spermatogenesis	Preserved	N.D.	N.D.	Preserved	N.D.	Preserved	Preserved	N.D.	N.D.	N.D.
Endocrine findings										
LH (basal)	Normal	Normal	Normal	Normal/low	Normal	Normal/low	Normal	Normal/low	Normal	N.E.
LH (GnRH stimulated)[d]	Low	Normal	High	Normal	Normal	Normal	N.E.	Low	N.E.	N.E.
FSH (basal)	Low	Low	Low	Low	Low	Normal/low	Normal/low	Low	Low	N.E.
FSH (GnRH stimulated)[d]	Low	Low	Low	Low	Low	Low	N.E.	Low	N.E.	N.E.
T (basal)	Normal/low	Normal	Normal/low	Normal/low	Normal	Normal/low	Normal	Normal/low	Low	N.E.
T (hCG stimulated)[e]	N.E.	N.E.	Normal	Normal	Normal	Normal	N.E.	Normal	N.E.	N.E.
E_1 (basal)	High	High	N.E.	High	High	High	High	High	High	N.E.
E_2 (basal)	Normal	High	High	Normal	High	Normal/high	High	High	High	N.E.
E_2 to T ratio	High	High	High	High	High	High	High	High	High	N.E.

E_1, Estrone; N.D., not determined; N.E., not examined.

[a] Detailed actual data are shown in Supplemental Table 1.

[b] A father-son pair.

[c] The sister has macromastia, large uterus, and irregular menses; the parental phenotype has not been described.

[d] GnRH 100 $\mu g/m^2$ (maximum 100 μg) bolus iv; blood sampling at 0, 30, 60, 90, and 120 min.

[e] hCG 3000 IU/m^2 (maximum 5000 IU) im for 3 consecutive days; blood sampling on d 1 and 4.

(assay no. Hs00903411_m1 for *CYP19A1*; Hs00324048_m1 for *DMXL2*; Hs00262671_m1 for *CGNL1*; Hs00833126_g1 for *MAPK6*; Hs00205710_m1 for *TMOD3*; Hs00322257_m1 for *TLN2*; and Hs99999910_m1 for *TBP*). The experiments were carried out three times.

Results

CYP19A1 mRNA levels and aromatase activities

Although relative mRNA levels of *CYP19A1* and catalytic activities of aromatase were grossly similar between LCL of case 3 (family A), case 4 (family B), and case 5 (family C) and those of control subjects, they were significantly higher in SF of case 3 (family A), case 4 (family B), case 9 (family D), and case 10 (family E) than in those of control subjects (Fig. 2).

Sequence analysis of *CYP19A1*

Direct sequencing showed no mutation in *CYP19A1* coding exons 2–10 of the 10 cases examined.

Genome structure analysis

CGH analysis revealed heterozygous cryptic duplications involving most of the *CYP19A1* exons 1 region in cases from families A and B, heterozygous cryptic deletions involving most of *DMXL2* and part of *GLDN* in cases from family C, and heterozygous cryptic deletions involving most of *DMXL2* in cases from families D–F (Fig. 3A). FISH analysis supported the duplications and confirmed the deletions.

Characterization of the cryptic duplications

Aberrant PCR products were obtained with the P2 primer (which amplifies a segment between exon I.1 and exon IIa with the P1 primer) and the P3 primer (which amplifies a segment between exon I.2 and exon I.6 with the P4 primer), and sequencing of the PCR products showed the same tandem duplication involving seven of the 11 exons 1 of *CYP19A1* in cases from families A and B (Fig. 3B). The duplicated region was 79,156-bp long, and the

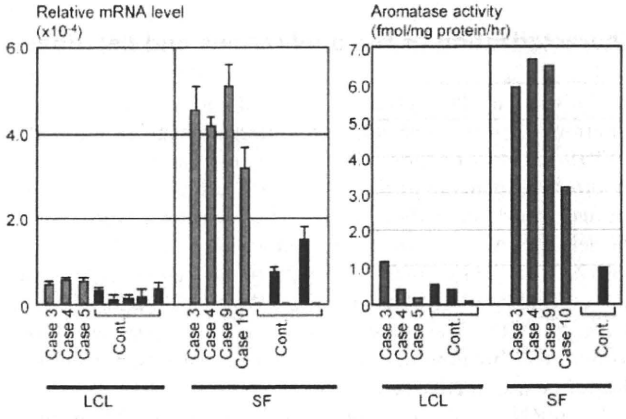

FIG. 2. Relative *CYP19A1* mRNA levels against *B2M* and catalytic activities of aromatase.

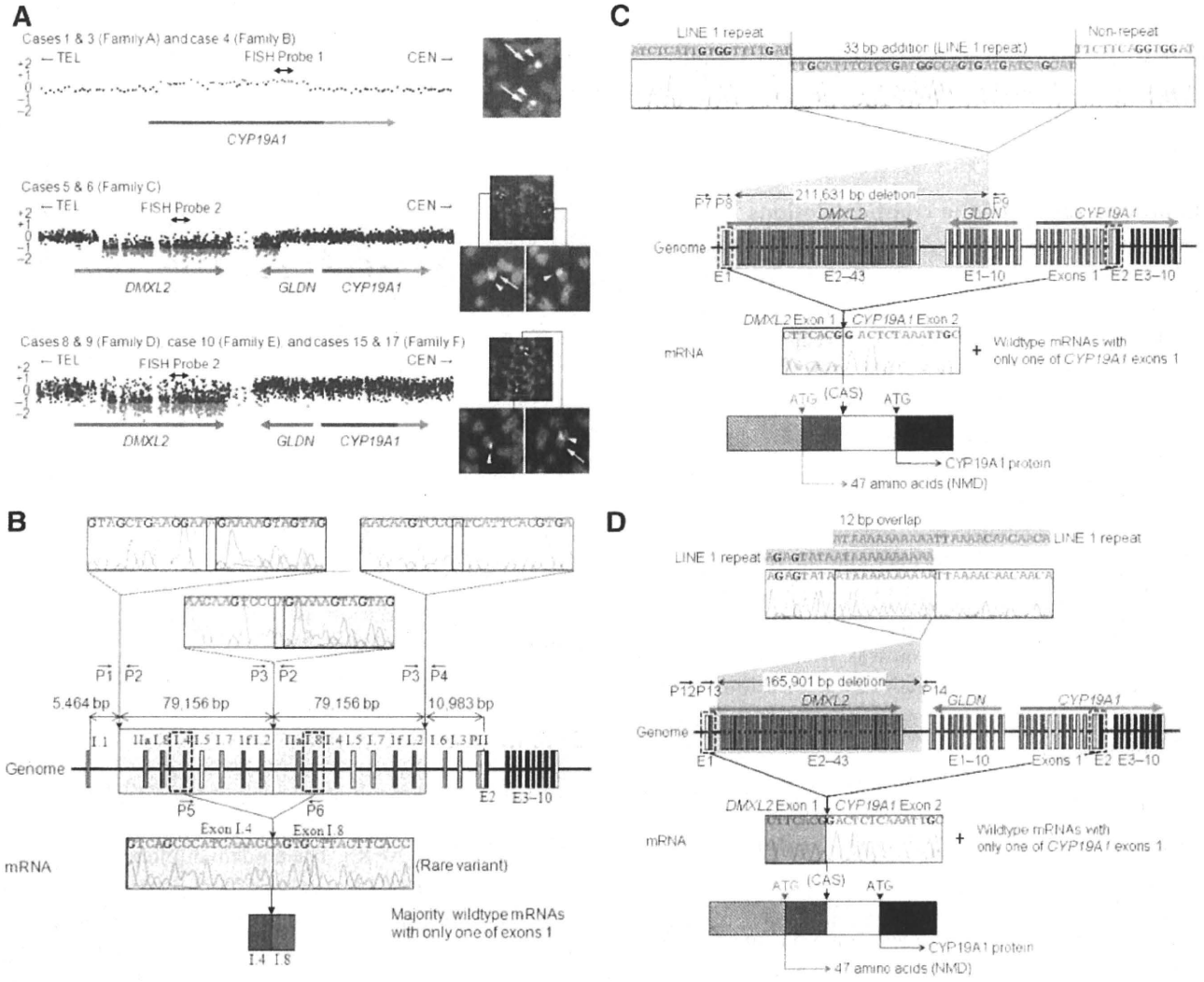

FIG. 3. Summary of molecular studies. For *CYP19A1*, the *dark* and *light blue lines* represent the genomic regions for noncoding exons 1 and coding exons 2–10, respectively. A, Oligoarray CGH and FISH analyses. In CGH analysis, the *black*, *red*, and *green dots* denote signals indicative of the normal, the increased (>+0.5), and the decreased (<−1.0) copy numbers, respectively. In FISH analysis, *two red signals* with an apparently different density are identified in cases from families A and B by FISH probe 1, whereas only a *single red signal* is found in cases from families C–F by FISH probe 2. The *green signals* are derived from the internal control probe. B, Schematic representation of the tandem duplication shared in common by cases 1 and 3 from family A and case 4 from family B. Genome, The junction sequence of the tandem duplication (*yellow boxes*) is shown, together with the original normal sequences at the 5′- and the 3′-ends of the duplicated region. The sequences highlighted with *light green* and *light orange* are identical, and 1 bp (A) is shared at the junction point (highlighted with *light yellow*). mRNA, The sequence of a rare clone is shown. The 3′-end of exon I.4 is connected with the 5′-end of exon I.8. C, Schematic representation of the deletion in sibling cases 5 and 6 from family C. Genome, The junction sequence of the deletion (*a gray area*) is shown. The fusion has occurred between a LINE 1 repeat sequence (*highlighted with blue*) at intron 1 of *DMXL2* and a nonrepeat sequence at intron 4 of *GLDN* and is accompanied by an addition of a 33-bp segment with a LINE 1 repeat sequence. mRNA, The sequence of a rare chimeric gene transcript is shown. *DMXL2* exon 1 consisting of a noncoding region (a *red striped box*) and a coding region (a *red box*) is spliced onto the common acceptor site (CAS) of *CYP19A1* exon 2 comprising an untranslated region (a *white box*) and a coding region (a *black box*). Thus, this transcript has two translation initiation codons (ATG), although the mRNA destined to produce a 47-amino acid protein from the ATG on *DMXL2* exon 1 is predicted to undergo NMD. D, Schematic representation of the deletion shared in common by cases 8 and 9 from family D, case 10 from family E, and cases 15 and 17 from family F. Genome, The junction sequence of the deletion (a *gray area*) is shown. The fusion has occurred between a LINE 1 repeat sequence (*highlighted with blue*) at intron 1 of *DMXL2* and that at a downstream region of *DMXL2*, with an overlap of a 12-bp segment. mRNA, The sequence of a chimeric gene transcript is delineated. The mRNA structure is the same as that described in the legend for Fig. 3C.

fusion occurred between nonrepeat elements with an overlap of one nucleotide.

All the 5′-RACE products (>500 clones) obtained from LCL and SF of case 3 (family A) and case 4 (family B) were found to be associated with a single exon 1, as observed in control materials. However, PCR amplifications for the 5′-RACE products with a variety of combinations of primers hybridizing to each exon 1 and subsequent sequencing of the PCR products revealed the presence of a chimeric clone consisting of exon I.4 at the 5′ side and exon I.8 at

the 3′ side in both LCL and SF (Fig. 3B). Although such a chimeric clone would have been produced by a splice error, this indicated that duplicated exon 1.4 at the distal nonphysiological position functioned as a transcription start site.

Characterization of the cryptic deletions

In cases from family C, long PCR products were obtained with the P7 primer and the P9 primer, and the deletion junction was determined by direct sequencing with the P8 primer (Fig. 3C). The deleted region was 211,631-bp long and involved exons 2–43 of *DMXL2* and exons 5–10 of *GLDN*. The two breakpoints resided within a LINE 1 repeat sequence and a nonrepeat sequence respectively, and a 33-bp segment with a LINE 1 repeat sequence was inserted to the fusion point. In cases from families D–F, long PCR products were obtained by sequential amplifications with the P12 primer and the P14 primer and with the P13 primer and the P14 primer, and an identical deletion was identified by direct sequencing with the P13 primer (Fig. 3D). The deletion was 165,901-bp long and involved exons 2–43 of *DMXL2*. The fusion occurred between two LINE 1 repeat sequences with an overlap of a 12-bp segment.

Sequence analysis of the 5′-RACE products obtained from LCL of cases 5 and 6 (family C) and from SF of case 9 (family D) and case 10 (family E) revealed the presence of a few clones with *DMXL2* exon 1 (2–5%), together with multiple clones with a single wild-type *CYP19A1* exon 1 (Fig. 3, C and D). Such a chimeric mRNA clone was absent from control materials. Furthermore, *DMXL2* exon 1 was found to be accompanied by a promoter-compatible sequence (Supplemental Fig. 2). This indicated a cryptic usage of *DMLX2* exon 1 as an alternative *CYP19A1* transcription start site in cases with deletions. Notably, because of the presence of the translation start codon on *DMXL2* exon 1, mRNAs of the *DMLX2/CYP19A1* chimeric genes are predicted to produce two proteins, *i.e.* CYP19A1 protein and an apparently nonfunctional 47-amino acid protein with a termination codon on *CYP19A1* exon 2, when the translation started from the initiation codons on *CYP19A1* exon 2 and on *DMLX2* exon 1, respectively. Furthermore, mRNA destined to yield the 47-amino acid protein is predicted to undergo nonsense-mediated mRNA decay (NMD) because it satisfies the condition for the occurrence of NMD (12).

Relative mRNA levels of *CYP19A1* and its neighboring genes

CYP19A1 showed a markedly high expression in the placenta and a relatively weak expression in a limited number of tissues including hypothalamus and ovary. By contrast, *DMXL2* was expressed in a range of tissues with some degree of variation as well as *CGNL1*, *MAPK6*, *TMOD3*, and *TLN2* (Fig. 4).

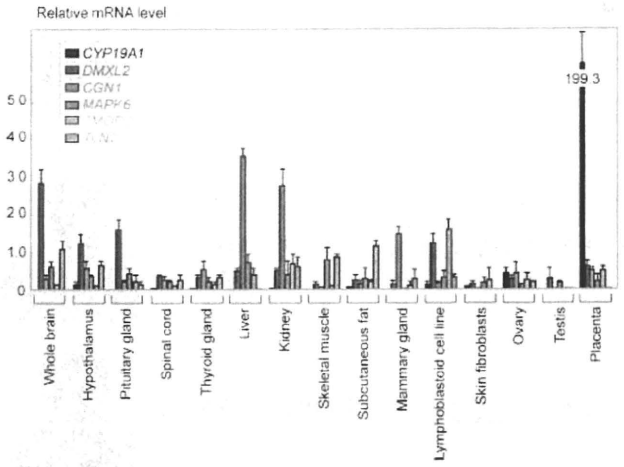

FIG. 4. Expression patterns of *CYP19A1* and the five neighboring genes involved in the chimeric gene formation. Relative mRNA levels against *TBP* are shown.

Discussion

We identified cryptic duplications of the *CYP19A1* promoter region and deletions of the *CYP19A1* upstream region in cases with AEXS. The tandem duplications would have caused *CYP19A1* overexpression because of an increased number of the wild-type transcription start sites. Indeed, because a rare mRNA variant with exon I.4 and exon I.8 was identified, this implies that duplicated exons 1 at the distal nonphysiological position can also function as transcription start sites. Similarly, the deletions would have caused *CYP19A1* overexpression because of a cryptic usage of *DMXL2* exon 1 with a putative promoter function as an extra transcription start site for *CYP19A1*. Indeed, because a few clones with *DMXL2* exon 1 and *CYP19A1* exon 2 were identified, this confirms the formation of a *DMXL2/CYP19A1* chimeric gene. Thus, our results suggest for the first time that duplications of a physiological promoter and deletions of an upstream region can cause overexpression of a corresponding gene and resultant human genetic disease.

Such cryptic genomic rearrangements can be generated by several mechanisms. The tandem duplication in families A and B would be formed by a replication-based mechanism of fork stalling and template switching that occurs in the absence of repeat sequences and is associated with microhomology (13). The deletion in family C is explained by nonhomologous end joining that takes place between nonhomologous sequences and is frequently accompanied by an insertion of a short segment at the fusion point (13).

The deletion in families D–F is compatible with a repeat sequence mediated nonallelic intrachromosomal or interchromosomal recombination (13). Thus, in conjunction with the previously identified four cryptic inversions that are also explainable by fork stalling and template switching or nonallelic recombination (8), genomic sequence around *CYP19A1* appears to harbor particular motifs that are vulnerable to replication and recombination errors.

To date, three types of cryptic genomic rearrangements have been identified in patients with AEXS, *i.e.* duplication type, deletion type (two subtypes), and inversion type (four subtypes) (Fig. 5). Here, although the deletion and the inversion types are associated with heterozygous impairment of neighboring genes (deletion or disconnection between noncoding exon(s) and coding exons), the phenotypes of patients are well explained by excessive *CYP19A1* activity alone. Thus, haploinsufficiency of these neighboring genes would not have a major clinical effect.

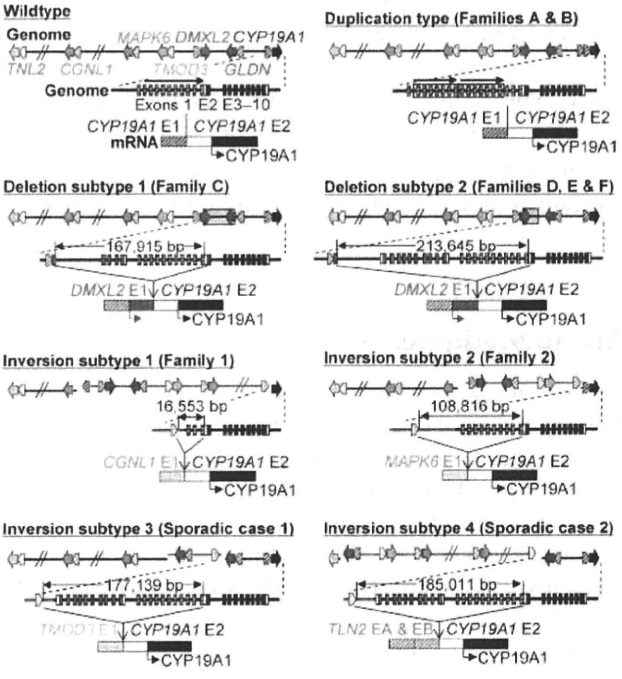

FIG. 5. Schematic representation of the rearranged genome and mRNA structures. The *white* and *black boxes* of *CYP19A1* exon 2 show untranslated region and coding region, respectively (for details, see Supplemental Fig. 1). For the duplication type and the deletion subtypes, see Fig. 3, C and D, for details. For genome, the *striped* and *painted arrows* indicate noncoding and coding exons, respectively (5′→3′). The inverted genomic regions are delineated in *blue lines*. For mRNA, *colored striped boxes* represent noncoding regions of each gene. For *TLN2*, exons A and B correspond to the previously reported exons 1 and 2 (8); because current exon 1 in the public database indicates the first coding exon, we have coined the terms exons A and B for the noncoding exons. The deletion and inversion types are associated with heterozygous impairment of neighboring genes [deletion or disconnection between noncoding exon(s) and the following coding exons]. The inversion subtype 1 is accompanied by inversion of eight of the 11 *CYP19A1* exons 1, and the inversion subtype 2 is associated with inversion of the placenta-specific *CYP19A1* exon I.1.

For the deletion and inversion types, two factors should be considered. One factor is expression patterns of each chimeric gene. In this regard, the five genes involved in the formation of chimeric genes are widely expressed, with some degree of variation (Fig. 4). Furthermore, *in silico* analysis revealed promoter-compatible sequences around exon 1 of *DMXL2*, *CGN1*, *MAPK6*, and *TMOD3* in multiple cell types, although such sequences remain to be identified for noncoding exons of *TLN2* (Supplemental Fig. 2). These findings imply that the chimeric genes show wide expression patterns because expression patterns of chimeric genes would follow those of the original genes.

The other factor is expression dosage of each chimeric gene. In this context, the *DMXL2/CYP19A1* chimeric mRNA was identified only in 2–5% of transcripts from SF, whereas the *CGNL1/CYP19A1* chimeric mRNA and the *TMOD3/CYP19A1* chimeric mRNA accounted for 89–100% and 80% of transcripts from SF, respectively (no data for the *MAPK6/CYP19A1* and the *TLN2/CYP19A1* chimeric genes) (5). This difference is obviously inexplicable by the relative expression level in SF that is grossly similar between *DMXL2* and *TMOD3* and is quite low for *CGNL1* (Fig. 4). In this regard, it is notable that a translation start codon and a following coding region are present on exon 1 of *DMXL2* (Fig. 5). It is likely that *DMXL2/CYP19A1* chimeric mRNA transcribed by the *DMXL2* promoter preferentially recognized the natural start codon on *DMXL2* exon 1 and underwent NMD and that rather exceptional chimeric mRNAs, which recognized the start codon on *CYP19A1* exon 2, were identified by 5′-RACE. By contrast, such a phenomenon would not be postulated for the inversion-mediated chimeric mRNA because of the absence of a translation start codon on the fused exon 1 of *CGNL1* and *TMOD3* (as well as exon 1 of *MAPK6* and exons A and B of *TLN2*) (Fig. 5). For the *CGNL1/CYP19A1* chimeric gene, furthermore, the physical distance between *CGNL1* exon 1 and *CYP19A1* exon 2 is short, and whereas a splice competition may be possible between exon 1 of neighboring genes and original *CYP19A1* exons 1, eight of 11 *CYP19A1* exons 1 including exon I.4 functioning as the major promoter in SF have been disconnected from *CYP19A1*-coding exons by inversion. These structural characters would have also contributed to the efficient splicing between *CGNL1* exon 1 and *CYP19A1* exon 2 (14). In this context, although the *CGNL1/CYP19A1* chimeric gene is associated with functional loss of eight *CYP19A1* exons 1 and the resultant reduction of *CYP19A1* expression in *CYP19A1*-expressing tissues, overall aromatase activity would be increased

by the wide expression of the chimeric gene. These structural properties would primarily explain the difference in the expression dosage of chimeric mRNA between the deletion and the inversion types.

It is inferred, therefore, that the duplication type simply increases *CYP19A1* transcription in native *CYP19A1*-expressing tissues, whereas the deletion and the inversion types cause relatively mild and severe *CYP19A1* overexpression in a range of tissues, respectively. These notions would grossly explain why clinical features of affected males and carrier females and endocrine profiles of affected males are apparently milder in the duplication and the deletion types than in the inversion type and why clinical findings were ameliorated with 1 mg/d of anastrozole in the duplication and the deletion types and with 2–4 mg/d of anastrozole in the inversion type. In addition, the different expression pattern between *CYP19A1* and *DMXL2* may explain, in terms of autocrine and/or paracrine effects, why phenotypic features such as gynecomastia tended to be more severe in the deletion type than in the duplication type under similar endocrine profiles.

Furthermore, several findings are notable in this study. First, a similar degree of FSH-dominant hypogonadotropic hypogonadism is present in the three types, with no amelioration of FSH responses to GnRH stimulation after GnRH priming in two cases with the duplication. This suggests that a relatively mild excess of circulatory estrogens, as observed in the duplication and the deletion types, can exert a strong negative feedback effect on FSH secretion, primarily at the pituitary, as has been suggested previously (15–19). Second, although basal T values appear to be mildly and similarly compromised in the three types, age-matched comparison suggests that T responses to hCG stimulation are apparently normal in the duplication and the deletion types and somewhat low in the inversion type. These data, although they remain fragmentary, would primarily be compatible with fairly preserved LH secretion in the three types and markedly increased estrogen values in the inversion type because T production is under the control of LH (1), and excessive estrogens compromise testicular steroidogenic enzyme activity (20, 21). Lastly, although testis volume appears somewhat small, fertility (spermatogenesis) is normally preserved in the three types. This would be consistent with the FSH-dominant hypogonadotropic hypogonadism because FSH plays only a minor role in male fertility (spermatogenesis) (22). Indeed, males with mutations of *FSHR* encoding FSH receptor as well as mice lacking *FSHB* or *FSHR* can be fertile (23, 24).

The results of this study are contrastive to those of the previous studies. In the previous studies, inversions only have been identified, and each inversion is specific to each family or patient (8). By contrast, in this study, the identical duplication was found in two Japanese families A and B, and the same deletion (subtype 2 in Fig. 5) was shared by three Japanese and one Caucasian families D–F, despite apparent nonconsanguinity. This may be explained by assuming that patients with severe phenotype were preferentially examined in the previous studies, whereas those with the AEXS phenotype were analyzed in this study without ascertainment bias. Furthermore, because phenotypes are milder in the duplication and the deletion types than in the inversion type, this may have permitted the spread of the duplication and the deletion types, but not the inversion type, as the founder abnormalities. This notion predicts that the duplication and the deletion types would be identified by examining patients with mild AEXS phenotype.

In summary, the present study shows that AEXS can be caused by duplications of the physiological promoters and microdeletions of the upstream regions of *CYP19A1* and that phenotypic severity is primarily determined by the tissue expression pattern of *CYP19A1* and the chimeric genes and by structural properties of the fused exons. Most importantly, the present study provides novel models for the gain-of-function mutations leading to human genetic disease.

Acknowledgments

Address all correspondence and requests for reprints to: Dr. Tsutomu Ogata, Department of Molecular Endocrinology, National Research Institute for Child Health and Development, 2-10-1 Ohkura, Setagaya, Tokyo 157-8535, Japan. E-mail: tomogata@nch.go.jp.

Present address for T.O.: Department of Pediatrics, Hamamatsu University School of Medicine, Hamamatsu 431-3192, Japan.

This work was supported by Grants for Research on Intractable Diseases (H22-035 and H22-098) from the Ministry of Health, Labor, and Welfare; Grants-in-Aid for Scientific Research (B) (20390265) and (S) (22227002) from the Japan Society for the Promotion of Science; and Grant-in-Aid for Scientific Research on Innovative Areas (22132004) from the Ministry of Education, Culture, Sports, Science, and Technology.

Disclosure Summary: The authors have nothing to declare.

References

1. **Bhasin S** 2008 Testicular disorders. In: Kronenberg HM, Melmed M, Polonsky KS, Larsen PR, eds. Williams textbook of endocrinology. 11th ed. Philadelphia: Saunders; 645–699
2. **Bulun SE, Takayama K, Suzuki T, Sasano H, Yilmaz B, Sebastian S**

2004 Organization of the human aromatase p450 (CYP19) gene. Semin Reprod Med 22:5–9
3. **Demura M, Reierstad S, Innes JE, Bulun SE** 2008 Novel promoter I.8 and promoter usage in the CYP19 (aromatase) gene. Reprod Sci 15:1044–1053
4. **Harada N, Utsumi T, Takagi Y** 1993 Tissue-specific expression of the human aromatase cytochrome P-450 gene by alternative use of multiple exons 1 and promoters, and switching of tissue-specific exons 1 in carcinogenesis. Proc Natl Acad Sci USA 90:11312–11316
5. **Shozu M, Sebastian S, Takayama K, Hsu WT, Schultz RA, Neely K, Bryant M, Bulun SE** 2003 Estrogen excess associated with novel gain-of-function mutations affecting the aromatase gene. N Engl J Med 348:1855–1865
6. **Binder G, Iliev DI, Dufke A, Wabitsch M, Schweizer R, Ranke MB, Schmidt M** 2005 Dominant transmission of prepubertal gynecomastia due to serum estrone excess: hormonal, biochemical, and genetic analysis in a large kindred. J Clin Endocrinol Metab 90:484–492
7. **Martin RM, Lin CJ, Nishi MY, Billerbeck AE, Latronico AC, Russell DW, Mendonca BB** 2003 Familial hyperestrogenism in both sexes: clinical, hormonal, and molecular studies of two siblings. J Clin Endocrinol Metab 88:3027–3034
8. **Demura M, Martin RM, Shozu M, Sebastian S, Takayama K, Hsu WT, Schultz RA, Neely K, Bryant M, Mendonca BB, Hanaki K, Kanzaki S, Rhoads DB, Misra M, Bulun SE** 2007 Regional rearrangements in chromosome 15q21 cause formation of cryptic promoters for the CYP19 (aromatase) gene. Hum Mol Genet 16:2529–2541
9. **Tiulpakov A, Kalintchenko N, Semitcheva T, Polyakov A, Dedov I, Sverdlova P, Kolesnikova G, Peterkova V, Rubtsov P** 2005 A potential rearrangement between CYP19 and TRPM7 genes on chromosome 15q21.2 as a cause of aromatase excess syndrome. J Clin Endocrinol Metab 90:4184–4190
10. **Stratakis CA, Vottero A, Brodie A, Kirschner LS, DeAtkine D, Lu Q, Yue W, Mitsiades CS, Flor AW, Chrousos GP** 1998 The aromatase excess syndrome is associated with feminization of both sexes and autosomal dominant transmission of aberrant P450 aromatase gene transcription. J Clin Endocrinol Metab 83:1348–1357
11. **Bellino FL, Osawa Y** 1977 Localization of estrogen synthetase in the chorionic villus fraction after homogenization of human term placenta. J Clin Endocrinol Metab 44:699–707
12. **Kuzmiak HA, Maquat LE** 2006 Applying nonsense-mediated mRNA decay research to the clinic: progress and challenges. Trends Mol Med 12:306–316
13. **Gu W, Zhang F, Lupski JR** 2008 Mechanisms for human genomic rearrangements. Pathogenetics 1:4
14. **Castillo-Davis CI, Mekhedov SL, Hartl DL, Koonin EV, Kondrashov FA** 2002 Selection for short introns in highly expressed genes. Nat Genet 31:415–418
15. **Shaw ND, Histed SN, Srouji SS, Yang J, Lee H, Hall JE** 2010 Estrogen negative feedback on gonadotropin secretion: evidence for a direct pituitary effect in women. J Clin Endocrinol Metab 95:1955–1961
16. **Belgorosky A, Guercio G, Pepe C, Saraco N, Rivarola MA** 2009 Genetic and clinical spectrum of aromatase deficiency in infancy, childhood and adolescence. Horm Res 72:321–330
17. **Alexander DC, Miller WL** 1982 Regulation of ovine follicle-stimulating hormone β-chain mRNA by 17β-estradiol *in vivo* and *in vitro*. J Biol Chem 257:2282–2286
18. **Mercer JE, Clements JA, Funder JW, Clarke IJ** 1988 Luteinizing hormone-β mRNA levels are regulated primarily by gonadotropin-releasing hormone and not by negative estrogen feedback on the pituitary. Neuroendocrinology 47:563–566
19. **Raven G, de Jong FH, Kaufman JM, de Ronde W** 2006 In men, peripheral estradiol levels directly reflect the action of estrogens at the hypothalamo-pituitary level to inhibit gonadotropin secretion. J Clin Endocrinol Metab 91:3324–3328
20. **Moger WH** 1980 Direct effects of estrogens on the endocrine function of the mammalian testis. Can J Physiol Pharmacol 58:1011–1022
21. **Strauss L, Kallio J, Desai N, Pakarinen P, Miettinen T, Gylling H, Albrecht M, Mäkelä S, Mayerhofer A, Poutanen M** 2009 Increased exposure to estrogens disturbs maturation, steroidogenesis, and cholesterol homeostasis via estrogen receptor α in adult mouse Leydig cells. Endocrinology 150:2865–2872
22. **Kumar TR, Wang Y, Lu N, Matzuk MM** 1997 Follicle stimulating hormone is required for ovarian follicle maturation but not male fertility. Nat Genet 15:201–204
23. **Tapanainen JS, Aittomäki K, Min J, Vaskivuo T, Huhtaniemi IT** 1997 Men homozygous for an inactivating mutation of the follicle-stimulating hormone (FSH) receptor gene present variable suppression of spermatogenesis and fertility. Nat Genet 15:205–206
24. **Layman LC, McDonough PG** 2000 Mutations of follicle stimulating hormone-β and its receptor in human and mouse: genotype/phenotype. Mol Cell Endocrinol 161:9–17

Insulin-Like Growth Factor I Enhances the Expression of Aromatase P450 by Inhibiting Autophagy

Bo Zhang, Makio Shozu, Masahiko Okada, Hiroshi Ishikawa, Tadayuki Kasai, Kouich Murakami, Kazuhito Nomura, Nobuhiro Harada, and Masaki Inoue

Department of Obstetrics and Gynecology (B.Z., M.O., T.K., K.M., K.N., M.I.), Kanazawa University Graduate School of Medicine, Kanazawa 920-0934, Japan; Reproductive Medicine (M.S., H.I.), Graduate School of Chiba University, Chiba 260-8670, Japan; and Department of Biochemistry (N.H.), School of Medicine, Fujita Health University, Toyoake, Aichi 470-1192, Japan

Aromatase, a key enzyme of estrogen biosynthesis, is transcriptionally regulated by many growth factors. IGF-I enhances aromatase activity in a variety of cells, but the mechanism of action has not been determined. We herein report our finding of a novel mechanism of action for IGF-I. IGF-I enhanced the dexamethasone (DEX)-induced aromatase activity by 30% in serum-starved THP-1 cells. The increase was associated with a corresponding increase in the level of aromatase protein but not with any change in the mRNA level. Metabolic labeling experiments revealed that IGF-I inhibited the degradation of aromatase. We identified pepstatin A as the most effective inhibitor of aromatase degradation by *in vitro* assay. Using a nontoxic concentration of pepstatin A, we examined IGF-I's action on aromatase distribution in microsomes and lysosomes. In the presence of pepstatin A, DEX caused an increase in the amount of aromatase in both microsomes and lysosomes, and IGF-I attenuated the DEX-induced accumulation of aromatase in lysosomes and, conversely, enhanced its accumulation in the microsomes. The addition of serum abolished the IGF-I-induced changes. The transport from microsome to lysosome was fluorescently traced in cells using a recombinant aromatase. IGF-I selectively reduced the aromatase signal in the lysosomes. Finally, we observed that IGF-I enhanced the aromatase activity by 50% as early as 1 h after treatment; furthermore, rapamycin, an enhancer of autophagy, completely negated the effect of IGF-I on the enzyme. These results indicate that IGF-I enhances aromatase by the inhibition of autophagy. (*Endocrinology* 151: 4949–4958, 2010)

Aromatase, a member of the P450 superfamily, is a key enzyme of estrogen biosynthesis and catalyzes the conversion of androgen to estrogen. Aromatase is expressed in the gonads, placenta, and other extraglandular tissues including adipose, breast, skin, brain, bone, arterial wall, liver, and uterus. All of these extraglandular tissues are estrogen receptor positive, and estrogen synthesized *in situ* is supposed to work directly on cells in a juxtacrine fashion. Currently, there is growing evidence that dysregulated expression of aromatase in these extraglandular tissues has pathological relevance and that targeting aromatase is an effective strategy for treatment of hormone-dependent tumors arising from these tissues, *i.e.* breast cancer, endometriosis, and leiomyoma of the uterus (1–5).

To understand the mechanisms responsible for the localized dysregulation (overexpression) of aromatase, researchers, including the authors of this paper, have extensively studied and found that a variety of tumor-derived humoral factors play pivotal roles in the localized induction of aromatase. For example, in breast cancer, malignant epithelial cells secrete significant quantities of prostaglandin E2, which induces transcription of aromatase in stromal cells surrounding breast cancer cells via the most proximal promoters of aromatase (promoter I.3 and PII) (6). Cytokines such as IL-6, oncostatin M, IL-11, TNFα,

ISSN Print 0013-7227 ISSN Online 1945-7170
Printed in U.S.A.

doi: 10.1210/en.2010-0294 Received March 11, 2010. Accepted June 29, 2010.
First Published Online July 28, 2010

Abbreviations: DEX, Dexamethasone; FBS, fetal bovine serum; GAPDH, glyceraldehyde-3-phosphate dehydrogenase; mTOR, mammalian target of rapamycin; PMSF, phenylmethylsulfonyl fluoride; RIPA, radioimmunoprecipitation assay.

and IL-1β stimulate aromatase transcription in stromal cells via a distal aromatase promoter (promoter I.4) (7–11) in the presence of circulating levels of glucocorticoids, which play a permissive role for the transcription (12). In addition to the transcriptional activation, TNFα and IL-11 can also enhance aromatase in breast cancer tissues by inhibiting the differentiation of aromatase-positive adipose stromal cells into aromatase-negative mature adipocytes (13).

IGF-I, a potent signaling molecule whose signaling pathway is implicated in the development and progression of a number of human neoplasms, including breast cancers (14), is also known to enhance aromatase. The precise mechanism is, however, still the subject of investigation. Unlike other factors that act in a cell- and promoter-specific fashion as described above, IGF-I consistently enhances aromatase in different types of cells (granulosa lutein cells, adipose stromal cells, skin fibroblasts, breast cells and breast cancer cells, and Leydig tumor cells) that use different types of aromatase promoters (15–19). Transcriptional activation through the induction of steroidogenic factor-1, a key transcription factor for the PII promoter, and indirect actions through the acceleration of follicular development and granulosa cell proliferation have been proposed as mechanisms of IGF-I's action in Leydig cells and granulosa cells, respectively (18, 20–22). These mechanisms explain the PII promoter-induced enhancement of aromatase in these cells but do not explain how IGF-I enhances aromatase in such a wide variety of cells that use different types of promoters.

We herein uncovered a novel mechanism whereby IGF-I enhances aromatase in a variety of cells, namely inhibition of autophagy. This action may explain the nonselective enhancement of ectopic expression of aromatase by IGF-I and its role in many human pathologies, including polycystic ovary syndrome and endometrial cancer, where free IGF-I and insulin are both high in serum (23, 24). This may also indicate the therapeutic relevance of a new class of anticancer drugs targeting mammalian target of rapamycin (mTOR), a gatekeeper of autophagy as well as cell proliferation (*i.e.* the use of an mTOR inhibitor may interfere with aromatase *in situ*).

Materials and Methods

Chemicals

IGF-I was purchased from R&D Systems (Minneapolis, MN). Dexamethasone (DEX) and all other chemicals, unless specifically indicated, were purchased from Sigma Chemical Co. (St. Louis, MO).

Cell culture

THP-1 (a human acute monocytic leukemia cell line) and JEG-3 cells (a human placental choriocarcinoma cell line) were purchased from the American Type Culture Collection (Rockville, MD) and cultured as described. For serum starvation, THP-1 cells were maintained for 6–24 h in RPMI 1640 medium supplemented with 0.1% BSA (albumin solution from fraction V from bovines; Sigma). The intrinsic aromatase-negative KW cells, previously established from an aromatase-positive myometrial cell line, were used for transfection experiments to trace extrinsic aromatase without interference from intrinsic aromatase (25–27).

Aromatase activity

Serum-starved THP-1 cells and KW cells were treated with IGF-I (5 ng/ml), DEX (25 nM), or both for 15 min to 48 h in RPMI 1640 medium supplemented with 0.1% BSA and 1β-[^{3}H]androstenedione (final concentration 60 nM; NEN Life Science Products, Boston, MA) was added to the medium 1 h before the end of incubation, unless otherwise specified. The aromatase activity was assayed by formation of tritiated water from 1β-[^{3}H]androstenedione as previously described (12, 28). The aromatase activity was expressed as the rate of formation of tritiated water per milligram of protein corresponding to 2 h of incubation.

Western blot

Western blotting was conducted as described previously (27). The polyclonal anti-aromatase antibody was obtained from the serum of rabbits immunized with placenta-derived aromatase (29). The antibody for P450 cytochrome oxidoreductase (CYPOR) was purchased from Santa Cruz Biotechnology (sc-25263; Santa Cruz, CA) and used to assure even loading of microsomal protein. The protein concentrations were determined by the bicinchoninic acid method (BCA Protein Assay Reagent, Pierce, Rockford, IL).

Quantification of aromatase mRNA

The aromatase P450 mRNA was measured by real-time PCR using primer pairs designed to amplify the exon 2–4 sequences as described previously (30). We also quantified the promoter-specific transcript levels of aromatase by exon-1-specific competitive RT-PCR using internal standard RNA as described previously (27, 31).

Aromatase expression vectors and transient transfection

The full-length aromatase cDNA was amplified from the pCMV-aromatase expression vector (pCMV-arom) (32) by PCR and was subcloned into the pcDNA3.1D/V5-His vector (pcDNA3.1D/V5-arom), in which a 14-amino-acid V5 epitope was added on the C-terminal end of the aromatase cDNA (pcDNA3.1 Directional TOPO expression kit; Invitrogen, Carlsbad, CA). The fidelity of the sequence was confirmed by sequencing.

Expression vectors were transiently transfected into KW cells using Superfect Reagent (QIAGEN, Valencia, CA) as described elsewhere (30, 33). The aromatase activity of the pCMV-arom- and pcDNA3.1D/V5-arom-transfected KW cells was examined by the tritiated water formation assay as described above.

Preparation of subcellular fractions

The cellular fractions of THP-1 cells were prepared by sequential centrifugations as described elsewhere (27). Briefly, cells were lysed on ice with buffer A [10 mM PBS, 15 mM KCl, 1 mM EDTA (pH 6.88)] and subsequently sonicated on ice. The lysate was centrifuged 10 min at 800 × *g* to remove nuclei, 10 min at 5000 × *g* to remove mitochondria, and 10 min at 10,000 × *g* to recover lysosomes as precipitates. The lysosome-rich precipitates were washed one time and solubilized using a modified radioimmunoprecipitation assay (RIPA) buffer [5 mM Tris, 1 mM EDTA, 1% Nonidet P-40 (pH 7.5)]. The supernatant was again centrifuged for 60 min at 105,000 × *g* to recover microsomes (27). The pellets were washed one time and resuspended in 50 μl buffer containing 50 mM PBS, 20% glycerol, 1 mM EDTA, and 1 mM dithiothreitol. Both microsomal and cytosolic fractions were snap-frozen in liquid nitrogen and stored at −80 C until use.

Placental tissues were obtained from patients, who gave the consent for the study, after normal delivery. The institutional review board approved this study. The placental tissues were homogenized, and microsome fractions were similarly prepared and stored at −80 C until use.

For detection of cellular aromatase, microsomal fractions were used for Western blotting. For detection of aromatase in the lysosome, crude lysosome fractions were refined by density-gradient centrifugation (lysosome enrichment kit; Pierce) to assure the subcellular localization.

^{35}S metabolic labeling experiments

THP-1 cells were pretreated with DEX (25 nM) in serum-free medium for 24 h. For pulse-labeling experiments, the cells were preincubated for 60 min in DMEM without methionine and cysteine supplemented with 0.1% BSA and were then pulse labeled for 60 min with 50 μCi/ml of Pro-Mix L-^{35}S *in vitro* cell labeling mix (GE Healthcare, Buckinghamshire, UK). ^{35}S-labeled cells were rinsed twice with PBS and incubated with regular RPMI 1640 culture medium (with 0.1% BSA) supplemented with cold methionine and cysteine (0.2 mM L-cystine HCl, 2 mM L-glutamine) with or without IGF-I (5 ng/ml). The cells were lysed with 1 ml modified RIPA buffer. The lysates were centrifuged at 10,000 × *g* for 10 min at 4 C, and the supernatants were used as the whole-cell extract. To remove any nonspecific proteins, 100 μl extract was gently mixed with 20 μl recombinant protein A agarose beads (protein A-Sepharose 4B conjugate; Invitrogen) and then incubated for 1 h at 4 C. The mixture was thereafter briefly centrifuged to remove the agarose beads; 0.5 μl rabbit polyclonal antihuman aromatase antibody, anti-β-actin antibody, and anti-glyceraldehyde-3-phosphate dehydrogenase (GAPDH) antibody were added to the supernatant; and the reaction was allowed to proceed with incubation at 4 C overnight with continuous agitation. After incubation, 20 μl agarose beads was added, and incubation was resumed for 1 h. The sample was centrifuged at 5000 × *g* for 1 min and the antigen-antibody complex-bound beads were saved and washed five times with modified RIPA buffer. The washed beads were suspended with 10 μl 2× SDS-PAGE sample buffer [125 mM Tris-HCl (pH 6.8), 10% 2-mercaptoethanol, 10% SDS, 10% glycerol] and boiled for 5 min. The extracted proteins were separated on a 10% SDS-polyacrylamide gel. Gels were dried and developed using the BAS 2000 system (Fujifilm, Tokyo, Japan). Radioactivity was expressed as the percentage of that at time zero.

In vitro degradation assay

The degradation of aromatase was assessed by the *in vitro* coincubation with fractionated cell lysates as a source of degradation enzymes. Placental microsomal fractions (1–5 μg protein) as a measure of crude aromatase were incubated with an aliquot of solubilized cellular factions (1.0 μg whole-cell homogenates, lysosome fraction, or cytosol fraction), prepared from JEG-3 cells or THP-1 cells. After an 8-h incubation at room temperature, residual aromatase protein was detected by Western blotting. Preliminary experiments showed that degradation proceeded most efficiently using a lysosomal fraction prepared from JEG-3 cells. The lysosome fractions were thus used for *in vitro* degradation assay.

Placental aromatase was stable in neutral to mild acidic conditions (pH 7.4–7.0) for at least 8 h at room temperature and was degraded by coincubation with lysosomal fractions in acidic conditions (pH ≤ 7.0). Degradation occurred more rapidly as the pH became more acidic, and acidic hydrolysis (a nonenzymatic mechanism resulting in degradation) became prominent under extremely acidic conditions (pH ~4.0). Therefore, the following experiments were conducted at pH 5.3 to minimize the contribution of nonenzymatic hydrolysis and maximize enzymatic digestion.

To identify the most effective inhibitors of degradation, the above assay was conducted in the presence of several type of inhibitors, including pepstatin A (an aspartate protease inhibitor), 3,4-dicholoroisocoumarin (a serine protease inhibitor), E64 (a cysteine protease inhibitor), aprotinin (a serine protease inhibitor), phenylmethylsulfonyl fluoride (PMSF, a serine protease inhibitor), sodium fluoride (an esterase inhibitor), sodium metavanadate (a phosphatase inhibitor), and MG132 (a proteasome inhibitor).

Detection of aromatase in subcellular fractions

The serum-starved THP-1 cells were treated with DEX (25 nM), IGF-I (5ng/ml), or both for 24 h in serum-free medium. Six hours before the end of the incubation, 0.1 mg/ml pepstatin A was added to the medium. The lysosomal and microsomal fractions were prepared and purified as described above in the presence of protease inhibitors (1 mM PMSF, 1 μg/ml aprotinin, and 1 μg/ul pepstatin A). The lysosomal fractions (0.3 μg protein per lane) and microsomal fractions (0.25 μg protein per lane) were then examined for aromatase expression by Western blotting.

Immunofluorescence staining

KW cells were grown on coverslips for 24 h and transiently transfected with pcDNA3.1D/arom-V5 plasmid (0.05 μg DNA per well of six-well plates) with 0.45 μg pUC19 DNA. After a 16-h recovery in complete medium containing 10% fetal bovine serum (FBS), the cells were fed with serum-free medium supplemented with 0.1% BSA for 6 h and thereafter with fresh serum-free medium containing IGF-I (5 ng/ml) for the last 24 h. Pepstatin A (0.1 mg/ml) and LysoTracker Red DND-99 (50 μM; Invitrogen), and ER-Tracker RED (glibenclamide BODIPY TR; Invitrogen) were added to the medium 6 and 1 h before the end of the incubation, respectively. Aromatase was stained using an anti-V5-fluorescein isothiocyanate antibody (Invitrogen). Briefly, the cells on the coverslips were fixed in 100% methanol for 5 min at room temperature and then subsequently with 1% BSA/PBS for blocking and finally were incubated with anti-V5-fluorescein isothiocyanate antibody diluted to 1:500 (Invitrogen). The cells

were imaged with an Olympus BX51 epifluorescence microscope. The images were captured with a charge-coupled device camera and the OpenLab software program (Nippon Roper, Tokyo, Japan) using a constant exposure time for each filter combination. Composite images were colored and assembled with Adobe Photoshop 5.5 (Adobe Systems, Mountain View, CA) with no alterations in the relative gray scale levels.

The aromatizing ability was confirmed by tritiated water released from 1β-[^{3}H]androstenedione in pcDNA3.1D/arom-V5-transfected KW cells.

Statistical analysis

Data are expressed as the means ± SEM unless otherwise specified. Differences in the transcription level and activity between the two groups were evaluated using the Mann-Whitney *U* test for unpaired data and Wilcoxon signed rank test for paired data. Statistical significance was established at the $P < 0.05$ level.

Results

IGF-I enhances aromatase activity without increasing the mRNA level

The aromatase activity of serum-starved THP-1 cells was measured in the presence or absence of IGF-I. IGF-I alone increased the basal level of aromatase activity by roughly 30% after 24 h of treatment (Fig. 1A). IGF-I similarly enhanced the DEX-induced level of aromatase activity by 30% (Fig. 1A). When the activity was assessed in the presence of DEX, the enhancement was significant at 12 and 24 h of IGF-I stimulation but was no longer significant by 48 h after initiation of treatment (Fig. 1B).

To clarify the mechanism by which IGF-I increases aromatase activity, the level of aromatase protein was quantitated by Western blot analysis at 24 h. IGF-I increased the amount of aromatase protein by 30% in the presence of DEX, which corresponded to the increase in its activity (Fig. 1C). To determine whether the increase in protein was due to increased transcription, the mRNA level of aromatase was subsequently measured by real-time RT-PCR. In contrast to the protein level, the mRNA level of aromatase did not show any increase in response to IGF-I, either in the presence or absence of DEX (Fig. 1D). The absence of any transcriptional influence of IGF-I was also confirmed by promoter-specific RT-PCR for aromatase.

This lack of effect on aromatase transcription was confirmed using KW cells, which were transiently transfected with pCMV-aromatase. IGF-I enhanced the aromatase activity without inducing a significant increase in aromatase transcription from the cytomegalovirus promoter-driven promoter (Fig. 1, E and F).

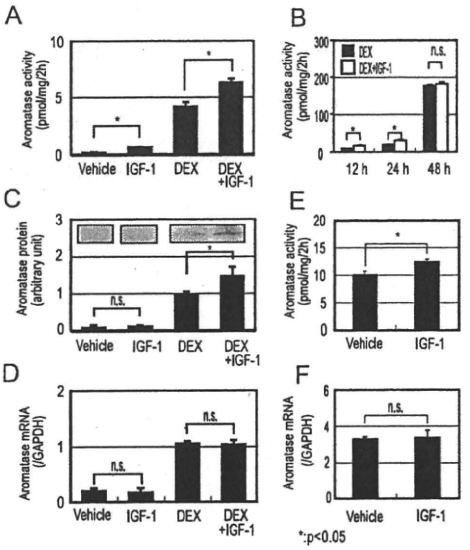

FIG. 1. The effect of IGF-I on the expression of aromatase in THP-1 cells. A, C, and D, The effect of 24 h IGF-I treatment on the activity (A), protein level (C), and coding mRNA level (D) of aromatase. Each *bar* represents the mean ± SEM of the values obtained from five independent experiments conducted in triplicate wells. The microsomal fraction was prepared by sequential ultracentrifugation and used for Western blot analysis. *Inset* images were taken from the same film. The amount of aromatase-coding mRNA was expressed as the ratio to GAPDH mRNA. Data represent the mean ± SEM of four independent experiments. B, The time course of the effects of IGF-I on aromatase activity. Data represent the mean ± SEM of four independent experiments. E and F, Effect of IGF-I on aromatase activity (E) and aromatase mRNA expression (F) in KW cells expressing pCMV-arom. After the recovery in complete medium for 12 h, transfected cells were starved for 6 h and then treated with IGF-I (5 ng/ml) for 20 h. Data were obtained from five independent experiments.

IGF-I stabilizes the aromatase protein

The coordinated increase in the protein and activity levels of aromatase (without a corresponding increase in the transcript level) suggested that IGF-I exerts its effects via a posttranscriptional mechanism. To confirm this hypothesis, the degradation of the aromatase protein was assessed by a ^{35}S metabolic labeling experiment. As shown in Fig. 2, A and B, IGF-I reduced the turnover of aromatase as early as 2 h after the initiation of treatment, and this effect continued for at least 6 h. GAPDH, a microsomal enzyme that is a target of chaperone-mediated autophagy, was similarly immunoprecipitated, and a degradation curve was produced for comparison purposes (Fig. 2C). The degradation curve of GAPDH was similar to that of aromatase under normal conditions, but IGF-I had no effect on GAPDH degradation.

Aromatase degradation is sensitive to pepstatin A

To determine the proteases responsible for aromatase degradation, we conducted an *in vitro* degradation assay and sought the most effective protease inhibitor(s). Pepstatin A efficiently inhibited aromatase degradation, whereas 3,4-dicholoroisocoumarin, E64, aprotinin, and PMSF did not. The inhibitory actions of sodium fluoride and sodium metavanadate were suboptimal. These results suggest that